Shape multistability in flexible tubular crystals through interactions of mobile dislocations

Andrei Zakharov[a,1] and Daniel A. Beller[a,b,1]

[a]Department of Physics, University of California, Merced, CA 95343; and [b]Department of Physics and Astronomy, Johns Hopkins University, Baltimore, MD 21218

Edited by Sharon Glotzer, Department of Chemical Engineering, University of Michigan, Ann Arbor, MI; received August 20, 2021; accepted December 5, 2021

We study avenues to shape multistability and shape morphing in flexible crystalline membranes of cylindrical topology, enabled by glide mobility of dislocations. Using computational modeling, we obtain states of mechanical equilibrium presenting a wide variety of tubular crystal deformation geometries, due to an interplay of effective defect interactions with out-of-tangent-plane deformations that reorient the tube axis. Importantly, this interplay often stabilizes defect configurations quite distinct from those predicted for a two-dimensional crystal confined to the surface of a rigid cylinder. We find that relative and absolute stability of competing states depend strongly on control parameters such as bending rigidity, applied stress, and spontaneous curvature. Using stable dislocation pair arrangements as building blocks, we demonstrate that targeted macroscopic three-dimensional conformations of thin crystalline tubes can be programmed by imposing certain sparse patterns of defects. Our findings reveal a broad design space for controllable and reconfigurable colloidal tube geometries, with potential relevance also to architected carbon nanotubes and microtubules.

elasticity | crystals | topological defects | dislocations

Diverse biological and synthetic systems at a range of scales are self-organized in ordered two-dimensional (2D) assemblies of cylindrical topology, including single-walled carbon nanotubes (SWCNTs) (1), filamentous viral capsids (2), microtubules (MTs) (3), and colloidal systems (4). Such tubular crystals frequently have circumferences of order only 10 times the interparticle spacing. This has the important consequence of restricting the orientations of the crystal axes, which trace out helical paths called parastichies, to a discrete set of possible angles with the tube axis. The number of distinct parastichies defines a pair of integer parastichy numbers, which index the possible crystalline tessellations of the cylinder, and which, for SWCNTs, determine the nanotube's electrical conductivity (5). The "parastichy" terminology arises from an intriguing connection with the botanical study of phyllotaxis, which examines plant structures with repeating patterns that follow parallel helices (or spirals); examples include the arrangements of seeds on a pine cone, scales on a pineapple, or leaves on a stem (6, 7).

Along with the importance of tubular crystals to molecular biology and the study of 2D solids, there is a growing interest in tubular crystals among soft matter physicists, due to the potential for exploiting phyllotaxis as a self-organization principle for colloidal particles or nanoparticles, and thus for creating assemblies of controllable helical pitch and chirality (4, 8–11). Higher-scale organization can occur through the coexistence of distinct phyllotactic tessellations on the same tube (12). Topological defects are central to this higher-scale organization: A change in parastichy numbers requires one or more dislocation defects at the boundary between domains (13). In SWCNTs, the analogous Stone–Wales defects in the honeycomb lattice of graphene are of great interest for their influence on plastic deformations (14) and electrical conductivity (5). Similarly, the observation of MTs with varying protofilament number (i.e., circumference) along their length implies the presence of dislocations in the rhombic packing of tubulin proteins (15).

Much of the recent work on frustrated phyllotactic self-organization has focused on particles constrained to lie in or adjacent to a fixed cylindrical surface (16–21). That version of the tubular crystal is realized in recent experiments on colloids confined in capillaries (4, 8, 22) or assembling on a cylindrical substrate (21), as well as a macroscopic "magnetic cactus" model system (23, 24). Tubular crystals on fixed cylinders exhibit a rich variety of phenomena such as oblique (rhombic) lattices (17), helical faults known as line slips (16), and individual dislocations behaving analogously to infinite grain boundaries (25).

However, in order to design colloidal analogs of MTs and SWCNTs, we must examine a different version of the problem, namely, the freestanding tubular crystal. Here, the particles are not constrained to any fixed surface; instead, the tubular surface emerges as the set of mechanical equilibrium positions of particles whose bond network has the topology of a tube (26). The ability of the tube shape to adapt locally and dynamically removes the source of frustration, specifically, the fixed circumference, that underlies the rich defect phenomenology of the fixed-cylinder crystals. On the other hand, this geometrical adaptability offers potential routes to stabilizing nontrivial tube shapes in the presence of defects, a possibility that has remained mostly unexplored.

In this work, we demonstrate, numerically, that freestanding tubular crystals possess controllable and composable mechanically multistable geometries, enabled by rearrangements of dislocations through glide mobility. This effect, which we refer to as

Significance

Crystalline sheets rolled up into cylinders occur in diverse biological and synthetic systems, including carbon nanotubes, biofilaments of the cellular cytoskeleton, and packings of colloidal particles. In this work, we show, computationally, that such tubular crystals can be programmed with reconfigurable shapes, due to motions of defects that interrupt the periodicity of the crystalline lattice. By identifying and exploiting stable patterns of these defects, we cause tubular crystals to relax into desired target geometries, a design principle that could guide the creation of versatile colloidal analogues to nanotubes. Our results suggest routes to tunable and switchable material properties in ordered, soft materials on deformable surfaces.

Author contributions: A.Z. and D.A.B. designed research; A.Z. performed research; and A.Z. and D.A.B. wrote the paper.

The authors declare no competing interest.

This article is a PNAS Direct Submission.

[1]To whom correspondence may be addressed. Email: azakharov@ucmerced.edu or d.a.beller@jhu.edu.

Published Febuary 2, 2022.

"dislocation-mediated shape multistability," operates through a costabilization of kinks in the tube axis with defect configurations that would be unstable on the fixed cylinder or the plane. While such kinks can also be formed with isolated disclinations (27, 28), our focus on dislocation pairs emphasizes mechanical shape reconfigurability through dislocation glide moves, which are purely local disruptions in the lattice. Recent experiments demonstrate that dislocations can be precisely generated and moved in 2D colloidal crystals using optical tweezers (29, 30) or local melting by a focused laser beam (31).

Using a minimal model of a tubular crystalline membrane, we show not only that a tubular crystal may possess distinct, mechanically stable geometries but also that it is possible to controllably switch between these competing states. Such switching can be achieved through quantitative changes in material properties, which, in principle, might be accomplished in situ by varying the temperature, or through application of external bending forces. Furthermore, by repeating certain stable dislocation motifs along the length of a tubular crystal, we show how multiple-kink structures approximating arbitrary curves can be targeted as equilibrium geometries, offering proofs of principle for large-scale shape manipulations of tubes into bent and helical structures.

The important distinction between freestanding and fixed-surface crystals is well known for the spherical topology, providing the difference between the scars of "spherical crystallography" (32) on rigid spheres and buckled crystalline shells resembling viral capsids (33) in flexible membranes. More generally, ordered soft matter confined to rigid, curved surfaces tends to relax the stresses imposed by Gaussian curvature through pair nucleation of topological defects (28, 34, 35); conversely, freestanding crystalline membranes can spontaneously adopt buckled geometries in the presence of defects such as dislocations and disclinations (36, 37). An analogous effect in nematic elastomer sheets allows for targeted shape transitions in the vicinity of a topological defect (38, 39), where nonzero Gaussian curvature arises to relax the elastic stresses.

At the same time, it is worth emphasizing key differences between tubular and spherical crystals. For spheres, topology demands a net excess disclination charge of +2, whereas tubes (even if closed as a torus) have no topologically required defects. In addition, the Gaussian curvature of surfaces such as spheres and tori can promote lines of dislocations known as scars (32) and stabilization of excess unbound disclinations (40). In contrast, the Gaussian curvature in a perfect cylinder is everywhere zero. Rather, defects in a tubular crystal are intimately related to the discretization of crystal axes orientations: A change of parastichy numbers, whether occurring spontaneously or to mediate plastic deformation, necessarily requires an intervening dislocation.

We study the emergent interplay of dislocation interactions and surface deformation geometries by modeling the crystalline membrane as a triangular-lattice network of harmonic spring bonds with a bending rigidity, and with the overall topology of a tube. We assume that dislocations glide freely into energy-minimizing configurations, with a rapid relaxation of the crystal's elastic energy between glide steps, and with a small, finite temperature able to overcome the Peierls barrier, which we ignore (26, 41). We prohibit climb motion for simplicity, with the justification that climb requires an exchange of mass with the surrounding medium along with breaking and forming of multiple bonds, a process typically much slower than glide relaxation (41). By this means, we calculate effective energy landscapes for dislocations interacting on a tubular crystal whose surface deformations respond strongly to changes in defect position, creating multistable energy landscapes in both defect configuration and tube shape.

Our approach extends the methodology widely used to create soft elastic actuators by encoding locally preferred membrane geometries in the in-surface order to develop target three-dimensional (3D) morphologies (42–44). Viewed as plastically deformed actuators, our shape-morphing tubular crystals represent potential routes to creating carbon nanotube actuators (45): metamaterials with exceptional mechanical properties (46), electronic behavior (47, 48), and biomedical potential (49, 50). Further, the metastable tubular crystals can be used as building blocks for larger-scale architected structures of different dimensionality, for example, yarns (51), ribbons (52, 53), or 3D networks (scaffolds) of connected tubules (54, 55). Our findings offer a potential mechanism for explaining and exploiting large deformations in tubular crystals at the nanoscale (56, 57). Defects in the tubulin lattice can significantly alter the mesoscale shape of an MT, and can provide a means of plastic deformation to accommodate external stress without breaking (58) or folding (59), and can even reinforce the structure (60).

Minimal Model of a Freestanding Tubular Crystal

We model the tubular crystal as a network of harmonic spring bonds l_{ij}, connecting massless nodes i, j, with a bending rigidity κ that penalizes deviations of the mesh from the preferred curvature. The network is six-coordinated, making a triangular lattice, everywhere except at elementary dislocations, where a five-coordinated positive disclination is adjacent to a seven-coordinated negative disclination. The discrete elastic energy associated with the stretching and bending of the mesh is defined as

$$\mathcal{F}^{\mathrm{d}} = \frac{\epsilon}{2}\sum_{\text{bonds}}(l_{ij}-a)^2 + \frac{\kappa}{2}\sum_{\text{nodes}}(4H_i^2 - 2K_i). \qquad [1]$$

The first term assigns a spring constant ϵ to deviations of bond length l_{ij} from rest length a. The second term assigns the bending rigidity κ to curvature distortions calculated from the discrete mean curvature H_i and discrete Gaussian curvature K_i at each node i (see *Materials and Methods* for details).

This free energy could represent a discretization of a continuum, isotropic elastic free energy for a membrane with Young's modulus $Y = 2\epsilon/\sqrt{3}$, Poisson ratio $\nu = 1/3$, and Lamé coefficients $\lambda = \mu = \sqrt{3}\epsilon/4$. However, throughout this work, we treat the nodes of the mesh as the inherently discrete particles that make up the phyllotactic tessellation. From Eq. **1**, along with the tube radius R and the proportionality of ϵ to Y, we obtain two important dimensionless parameters: the Föppl–von Kármán number $\gamma \equiv YR^2/\kappa$ and the reduced bending rigidity $\tilde{\kappa} \equiv \kappa/(Ya^2)$. The bending energy acts to increase the tube radius, creating a positive azimuthal strain u_{yy} and negative longitudinal strain u_{xx}, given at large γ by $u_{yy} = -u_{xx} \approx (1+\nu)/(2\gamma)$ (26). The optimal radius of the pristine tubular crystal is then $R \approx R_0(1 + u_{yy})$, where R_0 is the tube radius prescribed by minimizing the stretching energy alone. In the vicinity of a dislocation, deviations from a perfect cylindrical geometry are necessary to produce the expected surface buckling well known in planar 2D crystals (36).

The possible triangular lattice tessellations of a (quasi) cylindrical surface can be conveniently indexed using the botanically inspired parastichy numbers, a pair of integers (m, n) defining the number of distinct helices of particles in the steepest right-handed and steepest left-handed families, respectively, with the former family making an angle ϕ with the tube axis (Fig. 1). Conventionally, a third parastichy number $|m - n|$, determined by the other two, is often included (61). For a pristine (defect-free) tubular crystal, the radius in the limit of small κ is uniform throughout the tube and is given by

$$R \approx R_0(m,n) = (a/2\pi)\sqrt{m^2 + n^2 - mn}. \qquad [2]$$

However, for tubular crystals with defects, the tube radius is nonuniform, and we calculate a local R_i at each node i as the distance from a computed centerline (see *Materials and Methods* for details).

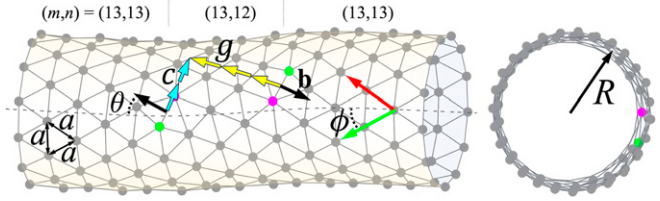

Fig. 1. A tubular crystal of radius *R*, preferred lattice spacing *a*, and helical angle ϕ that defines the deviation of the steepest left-handed helix (along the green arrow) from the tube axis (the dashed line). Light gray nodes each share a bond with six neighbors, whereas green and magenta nodes mark disclination sites with five or seven neighbors, respectively. Each five–seven disclination pair forms a dislocation, characterized by the Burgers vector **b** (black arrows) at angle θ to the tube axis. Each dislocation changes the parastichy numbers (m, n) by $\Delta m = \pm 1$ and/or $\Delta n = \pm 1$. The tube is flexible, and thus a defect creates deformations associated with change in the tube radius and a small reorientation in the tube axis. The two dislocations are separated by *g* glide steps (yellow arrows) and *c* climb steps (cyan arrows), respectively, along and perpendicular to **b**. The same crystal is shown from side (*Left*) and top (*Right*) views.

We consider elementary dislocations, each characterized by a Burgers vector $\mathbf{b}$, which has length a and is oriented orthogonally to the bond connecting the five–seven disclination pair (62) and parallel to one of the three parastichies passing through the dislocation site. The parastichy numbers (m, n) thus define six possible orientations for $\mathbf{b}$, each making a fixed angle $\theta = \phi + j \cdot 2\pi/6$, $j \in \mathbb{Z}$, with the tube axis.

We examine stability of dislocation positions with respect to glide motion, which carries a dislocation parallel to $\pm\mathbf{b}$ along one of the helical parastichies in discrete steps of size a. Dislocations with collinear Burgers vectors may sit on different parastichies, separated by climb motion normal to $\mathbf{b}$. Thus, in general, we can use the number of glide steps g and climb steps c separating the two parallel dislocations to parametrize axial separation $x = ca(\sqrt{3}/2)\sin\theta + ga\cos\theta$ and azimuthal separation $y = -ca(\sqrt{3}/2)\cos\theta + ga\sin\theta$ for a $(\mathbf{b}, -\mathbf{b})$ defect pair with orientations $(\theta, \theta + \pi)$ (Fig. 1).

In this work we choose a few representative (m, n) tessellations to explore in detail. Motivated by studies of MTs, which are tubular rhombic crystals of tubulin proteins most often comprising 13 protofilaments (63), we consider defects in tubular crystals with similar ratios of circumference to bond length: the zigzag achiral configuration $(m, n) = (13, 13)$ and the armchair achiral configuration $(m, n) = (14, 7)$. Our methods and qualitative findings can be extended to tubular crystals with other chirality, radius, or even lattice symmetry (64), presenting a broad design space for future investigations. In this work, we use our representative tubular crystals as test beds for a systematic construction of stable tube deformation geometries built up from dislocation pair interactions.

Kinked Tubes and Multistability in Defect Pair Interactions

We begin by examining stable configurations containing two interacting dislocations; these configurations will then be used as basic building blocks for more complex geometries. To avoid boundary effects, we assume that the dislocations are far from the ends of the tube compared to the characteristic length scale for interactions between a dislocation and a tube end, which we empirically observe to be quite small. For instance, at $\tilde{\kappa} = 0.1$, the in-plane and bending effective stresses exerted by a clamped wall on an isolated dislocation essentially vanish for separations larger than three lattice spacings. For simplicity, we choose the two Burgers vectors to be antiparallel to each other, $\mathbf{b}' = -\mathbf{b}$, so that a Burgers circuit enclosing both defects measures a vanishing total Burgers vector. The effective interaction energy of the dislocation pair depends on the separation x, y along the tube axis and the azimuthal direction, respectively, and on the Burgers vector inclination angles θ, $\theta' = \theta + \pi$ relative the tube axis. Dislocations initialized on the same glide parastichy may pair annihilate on reaching zero separation, $(x, y) = (0, 0)$, leaving a defect-free lattice at the energy minimum. This cannot occur for dislocations on different glide parastichies, because climb would be needed to achieve zero separation.

While an analytical treatment of defects in freestanding tubular crystals is beyond the scope of this work, we turn to analytical predictions for the fixed-cylinder case as a point of comparison (25). For general separations of a $\mathbf{b}, -\mathbf{b}$ dislocation pair on a fixed-cylinder tubular crystal, integration of the defects' stresses gives an effective interaction energy (25, 26)

$$\mathcal{F}_{\text{int}}(x, y, \theta) = \frac{Aa^2}{2}\left\{\ln[\cosh\tilde{x} - \cos\tilde{y}] + \tilde{x}\left[\frac{\sinh\tilde{x}\cos(2\theta) + \sin\tilde{y}\sin(2\theta)}{\cos\tilde{y} - \cosh\tilde{x}}\right]\right\}, \quad [3]$$

where $\tilde{x} \equiv x/R, \tilde{y} \equiv y/R$ are dimensionless quantities. Although this expression comes from a continuum elasticity calculation, it was found to agree well with simulations of fairly small cylindrical crystals (25). However, the fixed-cylinder case described by Eq. **3** has strictly zero Gaussian curvature and prohibits changes in tube radius that are energetically preferred when the phyllotactic indices change on either side of a dislocation, in accordance with Eq. **2**. In contrast, as we show below, a freestanding tubular crystal partially screens this interaction energy by kinking at the dislocation sites, resulting in defect pair interaction landscapes that can differ qualitatively from the fixed-cylinder prediction of Eq. **3**. It is also noteworthy that Eq. **3** is even in x, a symmetry that we will see is broken by the freestanding tube. We can expect to find significant deviations from Eq. **3** at defect separations on the order of $\sim R/\gamma^{1/4}$, which is the length scale over which surface deformations from one dislocation can influence the other dislocation (26).

As a first test case for dislocation pair interactions in the freestanding tubular crystal, we consider an $(m, n) = (13, 13)$ tube with reduced bending rigidity $\tilde{\kappa} = 0.1$ and with a dislocation pair described by Burgers vector orientations $(\theta, \theta') = \pm\pi/2$. The chosen dislocations are restricted to glide circumferentially along closed paths at constant x. In Fig. 2*A*, we plot the numerically calculated energy landscape as a function of axial and azimuthal separations x and y between the defects, with x held fixed in any one realization while glide alters y (dashed lines). It is immediately apparent from Fig. 2*A* that the stable y separations depend strongly on x, in a manner that lacks the $x \to -x$ symmetry of Eq. **3**. An energy gradient from positive to negative x arises from the bending energy's preference for dislocation motions that increase the tube radius (26); however, this gradient has no effect in our chosen example, because x is fixed.

Instead, we draw attention to the locations of energy minima along the glide lines of constant x. According to Eq. **3**, the fixed-cylinder case has no metastable states; there are either two equal minima, symmetrically placed around $y = 0$, for $|x| < \pi R/2$, or one minimum at maximal azimuthal separation $y = \pi R$ for $|x| > \pi R/2$ (Fig. 2 *A*, *Inset*). For the freestanding tube, we find a strikingly different energy landscape. At small $|x|$, the absolutely stable state is at $y = \pi R$, a configuration that the tube accommodates by taking on a double-kinked shape with oppositely oriented kinks at each dislocation (states 1 and 2 in Fig. 2*A*). Another pair of local minima, with smaller $|y|$ symmetrically placed about $y = 0$, are metastable. In these latter configurations, disclinations of like sign are close to each other (state 3 in Fig. 2*A*), generating similar local surface deformations whose overlap is costly; meanwhile, the tube axis remains approximately straight.

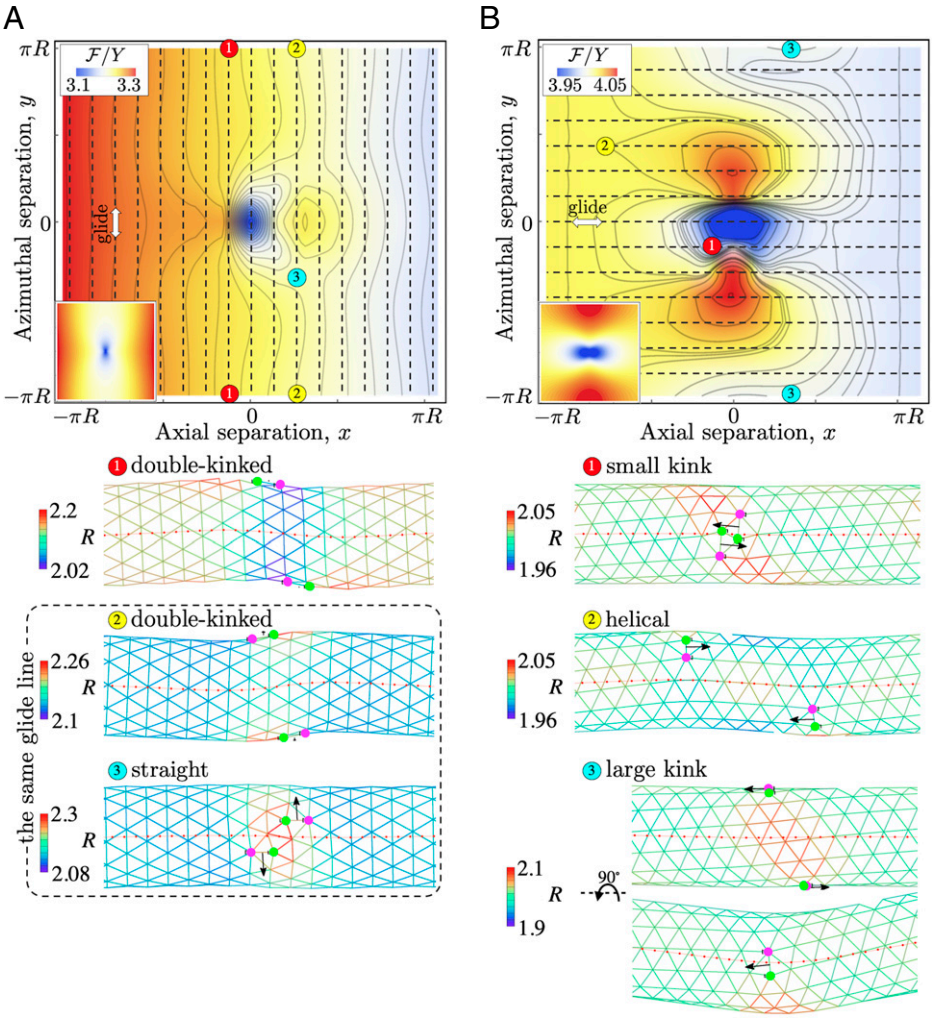

Fig. 2. Two interacting dislocation defects in a flexible tubular crystal ($\bar{\kappa} = 0.1$) with antiparallel Burgers vectors (black arrows) gliding (*A*) circumferentially at $\theta = \pi/2$ in a zigzag lattice $(m, n) = (13, 13)$ and (*B*) along the tube axis at $\theta = 0$ in an armchair lattice $(m, n) = (14, 7)$. The dashed lines in the energy landscapes (*Upper*) correspond to the glide parastichies, whereas solid lines show contours of the energy landscape. *Insets* in *Upper* are energy landscapes for a fixed-cylinder tubular crystal calculated using Eq. **3** (25). The 3D conformations (*Lower*), colored by a local measure of tube radius in units of the lattice spacing *a*, depict typical stable and metastable states marked in the energy plots.

Notably, the metastable states at small $|y|$ are not symmetric about $x = 0$. For $x < 0$, where the negative disclinations are nearer to each other (i.e., the positive disclinations are on the outside), the region between the dislocations has smaller radius and thus higher bending energy in the vicinity of the defects, which effectively makes the dislocations more attractive, whereas, for $x > 0$, the bending energy pushes the dislocations apart in order to enlarge the tube's wider central region.

At larger $|x|$ (where $y = \pi R$ is stable in the rigid-cylinder case), here the absolutely stable state switches from $y = \pi R$ to the small-$|y|$ pair of states. A contributing factor in this swap is the decreased repulsion between dislocations, owing to their overlapping surface deformations, as their $|x|$ separation increases. Gradually, on further increasing $|x|$, the $|y|$ locations of the absolutely stable states move out toward $|y| = \pi R$, eventually approaching the prediction of Eq. **3**. The special case of $x = 0$, for which dislocations could pair annihilate at $y = 0$, unsurprisingly has a global minimum at $y = 0$; but, more interestingly, there still exists a metastable state at $y = \pi R$ with a kinked tube axis. Overall, our calculations show, in this example, that the freestanding tubular crystal has a richer landscape of effective defect interactions, with less symmetry and new metastable states, as compared with the crystal on a fixed cylinder.

For another illustrative example of metastability in dislocation interactions, we next examine a dislocation pair gliding along the tube axis at $\theta = 0$, in an armchair lattice prescribed by $n = m/2 = 7$. Each dislocation now has fixed y and variable x. The choice $n = m/2$ minimizes $R(m, n)$ for a given m according to Eq. **2**, which diminishes the decrease in bending energy associated with tube-widening glide moves. Therefore, we expect that, for small $|x|$, the stretching energy will dominate over the bending energy. In this regime, do defects in the freestanding tubular crystal act as they do on a fixed cylinder? For the latter, the analytical solution (3) predicts a pair of energy minima symmetric about $x = 0$ for small fixed azimuthal separation y, whereas, for larger y, the dislocations repel indefinitely to large $|x|$ (Fig. 2 *B*, *Inset*). At $y = 0$, the defects attract each other and annihilate at $x = 0$. No metastable states are predicted at finite x.

Fig. 2*B* shows the energy landscape for the $\theta = 0$ dislocation pair in a freestanding tubular crystal. When both dislocations move along the same glide parastichy ($y = 0$), they attract and annihilate, as in the fixed-cylinder case. However, whereas the energy landscape for the fixed cylinder has a single global maximum at $(x, y) = (0, \pi R)$, here we see a pair of maxima at $x = 0$ situated near the $y = 0$ minimum. This has a few consequences for stability when we fix y in this landscape. The double minimum

configuration exists only at $y = -a\sqrt{3}/2$, causing only small deflections from the initial shape (state 1 in Fig. 2*B*). Meanwhile, a new metastable state arises at intermediate azimuthal separations, as the inward-shifted energy maxima present a barrier to the bending energy's push in the $+x$ direction (state 2 in Fig. 2*B*). The tube shape is helically deformed in these states, a generic consequence of kinks formed around defects at azimuthal separations neither zero nor πR. The energy barrier becomes smaller with increasing *y*, until, eventually, the barrier disappears, and the defects are able to glide freely to the tube ends, pushed by the bending energy to increase *R*. However, when the defects are located on opposite sides of the tube at $y = \pi R$, there exists another metastable state (state 3 in Fig. 2*B*), which creates a shape with a single large kink in the tube axis ($\sim 27^\circ$).

The kink angle caused by a single dislocation can be predicted based on the Burgers vector orientation θ and the tube radius *R*. The lattice contracts by one lattice spacing in the radial direction at $\theta = \pi/2$ with no change in chirality, and it shrinks by *a* in the longitudinal direction at $\theta = 0$. Since the longitudinal component of contraction, $a\cos\theta$, mainly contributes to the tube axis reorientation, a single dislocation causes a kink angle $\chi \approx \arcsin(a\cos\theta/(2R))$, which agrees well with the simulation results.

Extending this calculation to pairs of dislocations, we first note that two defects with parallel Burgers vectors on opposite sides of the tube cancel each other's effects on the tube axis orientation, whereas antiparallel **b** doubles the net kink angle. Defects at general azimuthal separation reduce each other's contributions to the kink angle by a factor proportional to $\cos(\beta)$, where β is the angle between the Burgers vectors of the two dislocation defects in the cylindrical projection of the tube into a plane. Thus, our prediction for the total kink angle reads $\chi_{\rm tot} \approx \arcsin(a\cos\theta/(2R))(1+\cos(y/R)\cos(\beta))$, which is in excellent agreement with the simulation results $\chi_{\rm tot} \approx 27.5^\circ$ at $\theta = 0$, $R \approx 2.1\,a$, $y = \pi R$, $\beta = \pi$, corresponding to state 3 depicted in Fig. 2*B*.

The two (m, n) examples we have presented so far reveal metastable states under dislocation glide that are unique to the freestanding tubular crystal. These states produce (and are stabilized by) kink-bent, double-kinked, or helically kinked tube conformations in competition with straight or nearly straight conformations.

Control Parameters for Multistability

We now demonstrate that our principle of dislocation-mediated shape multistability is versatile, as it can be controlled by a number of parameters. Some of these parameters could conceivably be changed dynamically during an experiment, such as through external forces or a temperature dependence of material constants.

Bending Rigidity. First, we examine how the energy barrier and the difference in energy between stable configurations depend on the reduced bending rigidity $\tilde{\kappa}$. Smaller $\tilde{\kappa}$ favors metastable states in two ways: by permitting localized tube deformations to accommodate nearby dislocations and by reducing the tube-widening stress that pushes defects to infinite separation. Thus, as we show below, changing $\tilde{\kappa}$ in situ can cause a snap-through transition between two (meta)stable tube shapes or destabilize a formerly metastable state.

Returning to the $(m, n) = (13, 13)$ tube, for two dislocations with azimuthally oriented Burgers vectors $(\theta, \theta' = \pm\pi/2)$ we test the multistability at $x = a\sqrt{3}$ noted above (states 2 and 3 in Fig. 2*A*) under changing $\tilde{\kappa}$. As shown in Fig. 3*A*, the configuration at separation $y = \pi R$, which is absolutely stable in a soft lattice at small $\tilde{\kappa}$ (red triangles in Fig. 3*A*), becomes metastable at intermediate $\tilde{\kappa}$ and then unstable when $\tilde{\kappa} > 0.25$, in favor of the competing stable configuration at small $|y|$. For comparison, we also show the corresponding calculation for the fixed-cylinder case: By constraining all particles to lie in a cylindrical surface, we obtain excellent agreement with the analytical prediction of Eq. **3** (open circles and black solid line in Fig. 3*A*). In this example, the fixed-cylinder crystal follows the trend observed with increasing $\tilde{\kappa}$ in the freestanding case, as $y = \pi R$ is highly unstable in favor of small $|y|$.

A similarly significant $\tilde{\kappa}$ dependence can be seen in the highly bent shape observed in the $(m, n) = (14, 7)$ tube for $\theta = 0$ and fixed $y = \pi R$, which, as noted above, has a metastable configuration at small, positive *x* (state 3 in Fig. 2*B*). We show, in Fig. 3*B*, that this state is very stable for small $\tilde{\kappa}$, then weakly metastable for intermediate $\tilde{\kappa}$, and, finally, unstable at large $\tilde{\kappa}$, requiring the defects to glide apart indefinitely. The fixed-cylinder analytical approach predicts a metastability near $x \approx -\pi R$, not seen in our simulations of freestanding tubes, due to an energy barrier centered at $x = 0$. Interestingly, the predicted $\mathcal{F}_{\rm int}$ from Eq. **3** retains starkly different stable states from the computed results even when we add a naïve version of the bending energy per unit length, $\mathcal{F}_b/L \to \pi\kappa/R$, using Eq. **2** for $R = R_0(m, n)$ with (m, n) changing abruptly at the *x* values of dislocations. The resulting total free energy prediction (green solid curve in Fig. 3*B*) is so different from the computed free energy at the same $\tilde{\kappa}$ that the positions of the maximum and the local minimum are almost swapped.

So far, we have examined only azimuthal and axial glide trajectories, but shape multistability arises also in the more generic case of glide along helical parastichies. As an example, we turn to the case of $\theta = \pi/6$ in the $(m, n) = (13, 13)$ tube, with constant climb separation $c = 2$. We find a local energy minimum at $x \approx -\pi R$ (Fig. 3*C*), in which the tube morphs into a helical shape, whereas a straight shape is recovered if the defects surmount an energy barrier at small $|x|$ to glide indefinitely toward $x \to +\infty$. This energy barrier increases with decreasing $\tilde{\kappa}$, and, similarly to the $\theta = 0$ case, the metastable state can be attained only if the initial separation $x < -\pi R/2$.

If we instead choose $c = 0$, allowing dislocation pair creation or pair annihilation, there is an energy barrier at small $|x|$ that divides a short-ranged attractive region, dominated by the stretching energy, from a long-ranged repulsive region, dominated by the tube-widening stress from the bending energy (red triangles in Fig. 3*D*). Indeed, our naïve bending energy term summed with the analytical stretching energy of Eq. **3** fits the data very well (red line in Fig. 3*D*). However, this agreement breaks down qualitatively at smaller $\tilde{\kappa}$, where the analytical approach predicts attraction at all *x* due to the weakened repulsive influence of the bending energy (green and black solid lines in Fig. 3*D*). Instead, the computed results for the freestanding tube show that the dislocations become weakly repulsive for separations beyond just a few glide steps (green and black triangles in Fig. 3*D*). Evidently, the freedom to deform from the cylindrical reference state allows the freestanding tubular crystal to partially screen the interactions predicted by Eq. **3**.

External Bending Stress. Externally imposed stresses present another set of routes to switching a freestanding tubular crystal between different (meta)stable states. Here we focus on external bending stress as a means of overcoming the energy barriers described above. The timescale for these switches is that of several glide steps, which we assume to be rapid enough to be observable (65). We take, as initial states, some of the stable states identified above. To apply bending stress, the edge at one end of the tube is held fixed (taken to be clamped) while the other end is displaced from its reference position by distance *d*, producing curvature along the tube of $\sim 2d/L^2$.

We first choose an angle ψ in the *YZ* plane to give, along with the initial tube axis *X*, a plane of bending, such that compression is maximum along the direction picked out by ψ. For

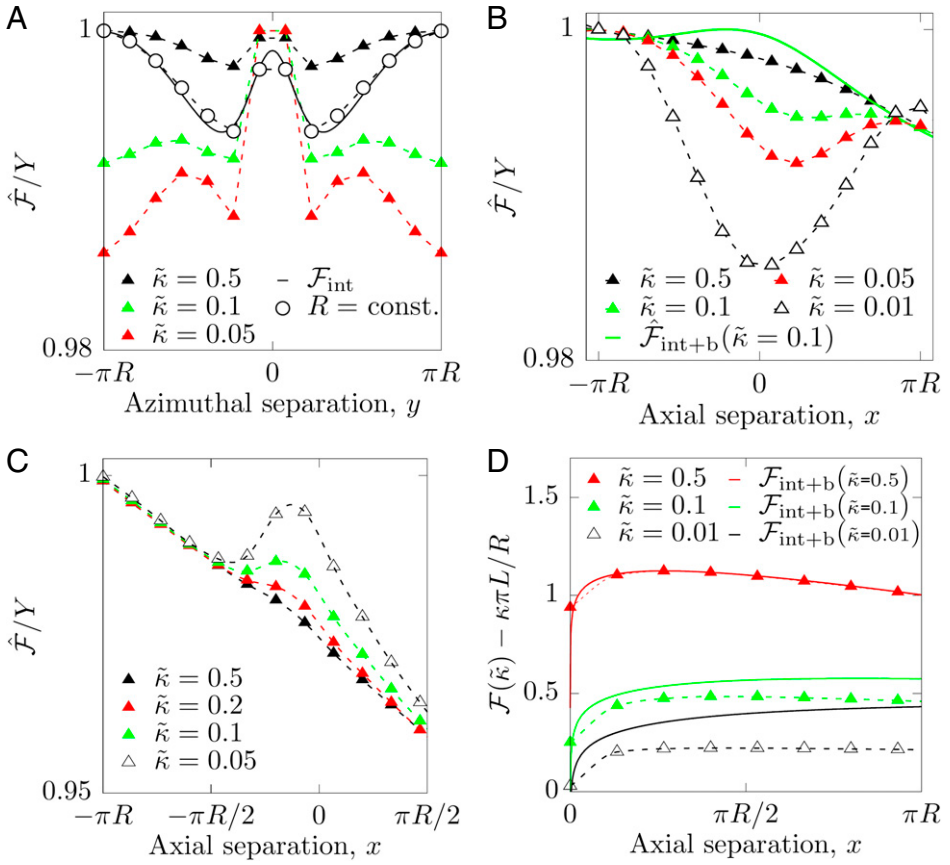

Fig. 3. Energy profiles for two interacting, gliding dislocations, at varying values of reduced bending rigidity $\tilde{\kappa}$, with (*A*) $\theta = \pi/2$ and $x = a\sqrt{3}$ in an $(m, n) = (13, 13)$ tube, (*B*) $\theta = 0$ and $y = \pi R$ in an $(m, n) = (14, 7)$ tube, and (*C*) $\theta = \pi/6$ and $c = a\sqrt{3}$ climb steps separation in an $(m, n) = (13, 13)$ tube. The energy is normalized to a rescaled energy $\hat{\mathcal{F}}/Y$ in each plot such that the largest value is one. (*D*) Dislocations moving along the same glide parastichy at $\theta = \pi/6$ in the $(m, n) = (13, 13)$ tube are attractive only at small separation and then become repulsive (triangles), whereas a naïve analytical approach (solid curves) predicts pair annihilation from any initial separation for small $\tilde{\kappa}$.

convenience, we take $\psi = 0$ to be the average initial azimuthal position of the two dislocations. Then we incrementally increase the imposed bending curvature from zero, checking the stability of both dislocations at each increment and performing glide steps whenever this lowers the total energy. For each bending direction ψ, we thus find the critical curvature at displacement d^* that destabilizes the initial defect configuration.

A particularly interesting case in which to study imposed bending is that of $(m, n) = (13, 13)$, $\theta = \pi/2$, and $c \neq 0$, as the dislocation pair can neither reach zero separation nor glide apart beyond a certain maximum distance. We found above that a pair of small-$|y|$ stable states, causing a nearly straight tube shape, are accompanied at smaller $\tilde{\kappa}$ by a stable state at $y = \pi R$, which gives the tube a double-kinked shape (Fig. 3*A*). The straight and double-kinked shapes have approximately equal energy at $\tilde{\kappa} = 0.1$. Using this value of $\tilde{\kappa}$, in Fig. 4*A*, we examine a tube with two dislocations at a small climb separation $c = 2$, $x = a\sqrt{3}$, and an initially small azimuthal separation corresponding to one of the stable straight shapes (state 1). We find that the applied curvature necessary to enable the dislocations to glide apart, and produce the double-kinked shape (state 2), is highly dependent on bending direction ψ; for a large ψ interval, the straight shape remains stable even at large applied curvature (state 3). For other ψ values, bending easily produces a double-kinked shape which, by virtue of its energetic stability, persists when the applied stress is removed. Moreover, imposing even large bend in any other direction does not lead to a reverse transition. Instead, the separation between dislocations remains constant, and both defects glide simultaneously until reaching the bending plane. This enables the tube shape to adapt to the applied bend by reorienting the kink in the energetically preferred tube axis (for example, as shown in state 2). Thus, the position of defects can be controlled by changing ψ.

Interesting similarities and differences in this direction-dependent response to bending are seen when we examine the singly kinked shape at $(m, n) = (14, 7)$, $\theta = 0$, $x = 0$, $y = c = \pi R$, $\tilde{\kappa} = 0.1$ (state 1 in Fig. 4*B*), which already resembles a bent configuration even without external forces. In this case, for all values of ψ, a finite applied curvature is found at which the $x = 0$ state becomes unstable; the dislocations then glide apart to the ends of the tube, leaving behind no defects and thus a straight tube shape. However, the kinked shape is much more easily destabilized at $\psi = 0$ or π, when the dislocations are $90°$ away from the bending plane, than at $\psi = \pm\pi/2$, when the dislocations are in the bending plane. A similar transition to a defect-free state from a helical shape takes place in an $(m, n) = (13, 13)$ tube with defects at $\theta = \pi/6$ and short separation (Fig. 4*C*). Since the shape is helical, this case lacks the $\psi \to -\psi$ symmetry seen in Fig. 4*B*. Taken together, the results in Fig. 4 suggest that the ψ dependence of d^* changes smoothly with θ, such that the sharp peak at $\psi = \pi/2$ remains while the peak at $\psi = -\pi/2$ diminishes and finally disappears as θ increases from zero to $\pi/2$.

Effect of Spontaneous Curvature. So far, we have assumed that the crystal has no spontaneous curvature, meaning that its ground state would be planar if it were "unzipped" from its cylindrical topology. But a spontaneous mean curvature clearly aids the assembly of a tube from a sheet, so it is important to address

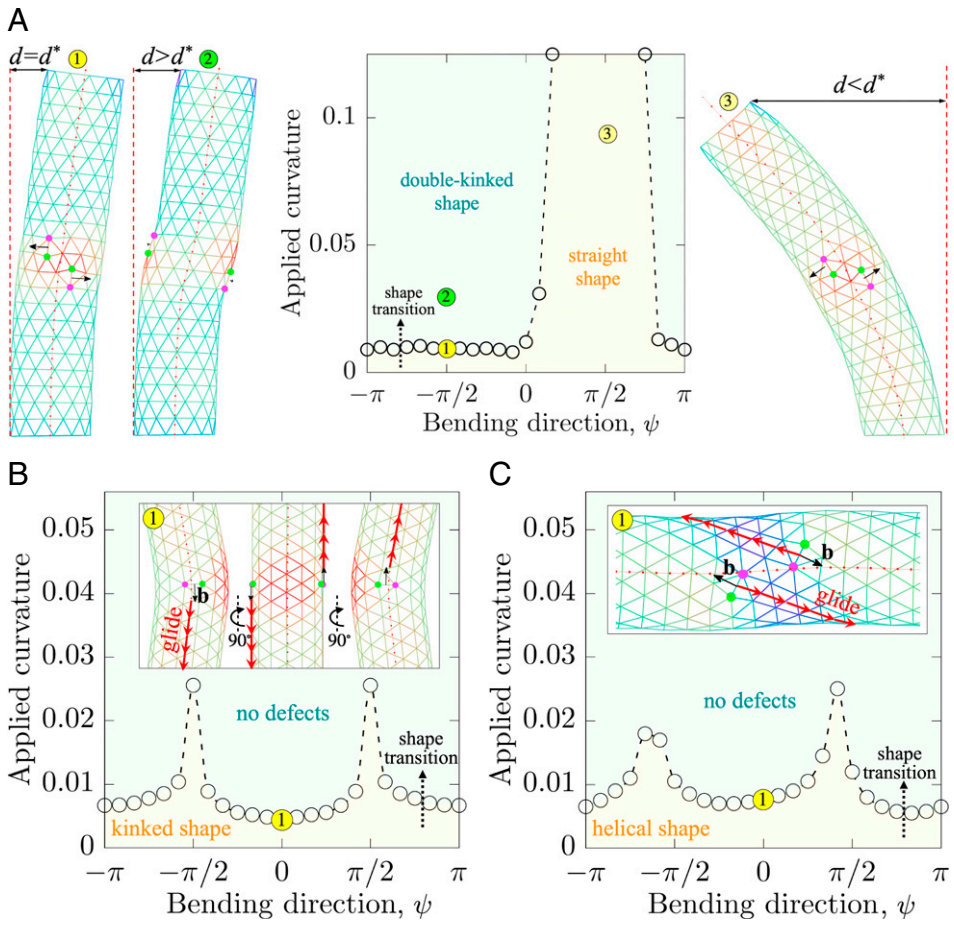

Fig. 4. Shape transition between stable states depending on the orientation ψ and magnitude (transverse displacement d) of applied bending strain at $\tilde{\kappa} = 0.1$. Here $\psi = 0$ corresponds to the average azimuthal position of the two dislocations being located on the compressed side of tube. The open circles (with dashed lines as guides to the eye) correspond to the critical displacement d^* at which the shape change occurs. The dotted arrows show an irreversible transition from the initial metastable state below the critical curvature (yellow region) to the final stable state (green region) of a different shape. The transition is qualitatively the same at all ψ. Representative shapes at particular choices of ψ are shown in the corresponding numbered images. The red arrows in *Insets* of *B* and *C* depict the glide parastichies. (*A*) $\theta = \pi/2$ with $(m, n) = (13, 13)$, (*B*) $\theta = 0$ with $(m, n) = (14, 7)$, and (*C*) $\theta = \pi/6$ with $(m, n) = (13, 13)$.

how such a material property will affect defect-mediated shape multistability. A plausible mechanism for such spontaneous curvature in MTs is the presence of additional proteins that bind to adjacent protofilaments and change the angle at lattice contacts (66). This provides anisotropic spontaneous curvature, with different preferred curvatures along principal directions. We similarly impose spontaneous curvature $1/R_0$ along one principal direction of the crystalline membrane, whereas the spontaneous curvature remains zero along the other direction, so that the bending energy is minimized in the initial, cylindrical state of a pristine tubular crystal. Details of the numerical implementation are described in *Materials and Methods*.

In Fig. 5, we illustrate with two examples that spontaneous curvature may change which of the tube shapes are stable and thus offers another potential control parameter. Without spontaneous curvature, two dislocations in an $(m, n) = (13, 13)$ tube, oriented at $\theta = \pi/2$ and separated by $x = -a\sqrt{3}$, have two stable states (mirror reflections of each other) at short azimuthal separation (Fig. 2*A*) that lead to a helical shape (state 1 in Fig. 5*A*). Adding spontaneous curvature $1/R_0$ causes a transition to an absolutely stable double-kinked shape with defect separation $y = \pi R$. Another effect of spontaneous curvature is shown in Fig. 5*B* for a tube with defects gliding along the tube axis at $\theta = 0$, $y = \pi R$. The spontaneous curvature stabilizes the metastable state at small x by increasing the energy barrier and reducing the bending energy loss due to glide (i.e., the slope of the energy's dependence on x is decreased). However, the global minimum energy state is still the defect-free configuration occurring at $|x| \to \infty$, which can be reached, for example, by applied bending. Comparing Fig. 5

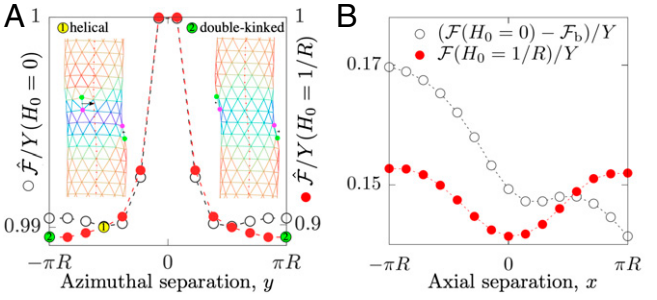

Fig. 5. Spontaneous curvature changes the optimal separation between two interacting dislocation defects, triggering a transition between stable helical and double-kinked shapes. Plots show the energy's dependence on the separation between dislocations for a tubular crystal of radius R without (empty black circles) and with (filled red circles) spontaneous curvature $H_0 = 1/R$, with $\tilde{\kappa} = 0.1$, at (*A*) $\theta = \pi/2$, $x = -a\sqrt{3}$, $(m, n) = (13, 13)$ and (*B*) $\theta = 0$, $y = \pi R$, $(m, n) = (14, 7)$. The bending energy of constant value $\mathcal{F}_b$ for a pristine tube is subtracted, in *B*, from the total energy for the $H_0 = 0$ case in order to plot the considered cases on the same scale.

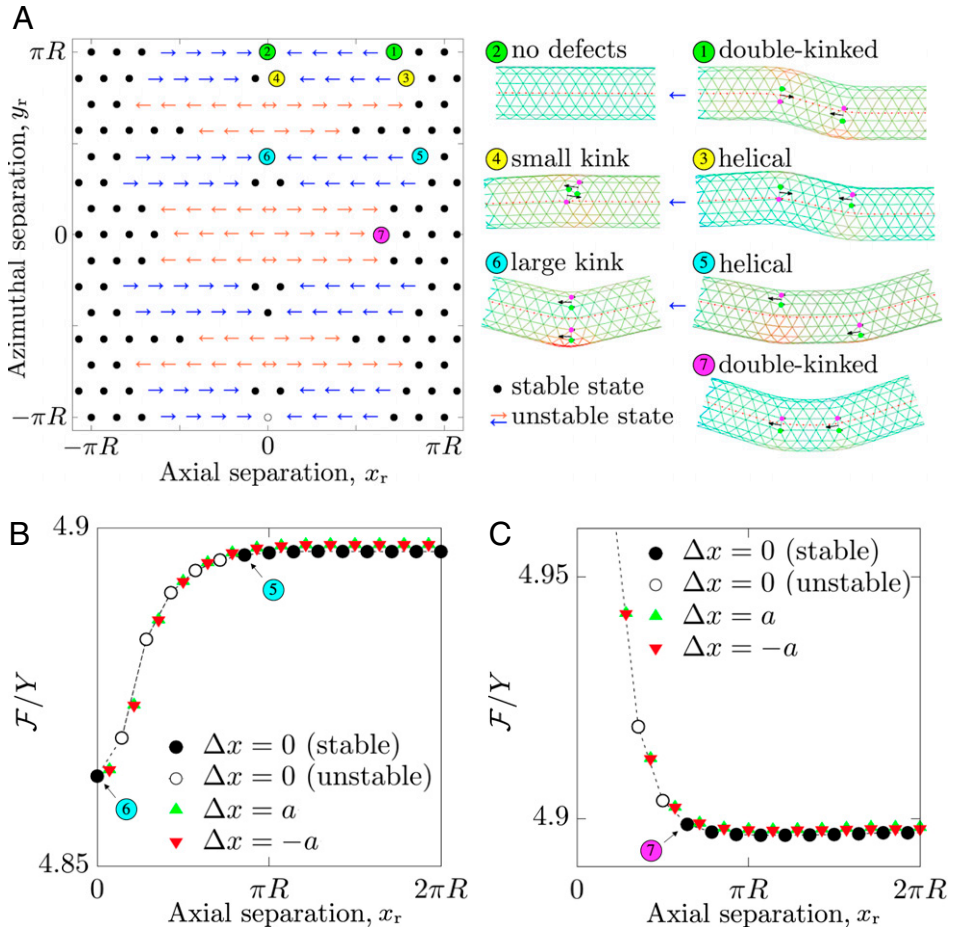

Fig. 6. Stability of two pairs of dislocations gliding in an $(m, n) = (14, 7)$ armchair tube with $\tilde{\kappa} = 0.1$. (*A*) Stable (black dots) and unstable (arrows) relative displacements between the two dislocation pairs, with a locally stable $y = \pi R$, $x = 0$ separation between the two dislocations within each pair. Collectively stable states exist at all possible relative azimuthal separation y_r at large relative separation x_r along the tube axis, but become unstable when separation x_r decreases, demonstrating attraction (blue arrows) to the absolutely stable state at small separation or repulsion (orange arrows) to larger separation. The 3D tube conformations are shown for several representative stable configurations on the right. (*B*) Energy profile for gliding at constant azimuthal separation $y_r = 3a\sqrt{3}/2$ between glide parastichies. At large x_r, a glide step of either dislocation in the moving pair (red and green triangles) is unfavorable unless its partner glides in the same direction, giving a series of metastable states (solid black circles). Decreasing the x_r separation eventually leads to consecutive unstable states (open circles) as the two dislocation pairs attract toward the global minimum at $x_r = 0$, which gives the tube a large kink. Selected corresponding tube conformations are depicted in *A*. (*C*) Two dislocation pairs on the same glide parastichies at constant $y_r = 0$. Pairs are stable (solid black circles) at large x_r and repulsive at small x_r separation (open circles). Metastable shape with shortest separation is shown in *A*.

to Fig. 3 *A* and *B*, we see that the introduction of spontaneous curvature has an effect similar to decreasing $\tilde{\kappa}$, with regard to which defect separations are stabilized or destabilized. This can be rationalized by recognizing that the reference state is now a minimum of the bending energy, so the energy penalty for deviations from the reference state is of higher order in small bending distortions compared with the case of zero spontaneous curvature, which is always far from its locally preferred minimum.

We anticipate that spontaneous curvature also changes effective defect interactions in a manner similar to varying $\tilde{\kappa}$ for other choices of Burgers vector orientation θ and phyllotactic indices (m, n). We leave for future work the computation of full energy landscapes at a range of H_0 values, examining here only two special configurations. Spontaneous curvature can also change locally and temporally in realistic scenarios, for example, with temperature or with concentration of binding proteins (67, 68), providing an additional way to control defect interactions and stable shapes.

Designing Target Shapes via Metastability and Buckling

We now build hierarchically upon our findings for dislocation pairs to study interactions among multiple pairs of dislocations, as routes to targeting desired tube shapes over larger length scales. As we have shown, two dislocations with parallel gliding directions can be attracted to a number of possible stable configurations, depending on their climb separation and Burgers vector orientations, that significantly change the macroscopic shape of the tube. The main shape motifs we have found are kinked, double-kinked, helical, and (nearly) straight. We here take these shape elements as building blocks of programmable and switchable geometries at mechanical equilibrium.

Because a generalization to interactions of arbitrarily many defects is impractical, we proceed by examining interactions of pairs of dislocation pairs, with each $\mathbf{b}$,$-\mathbf{b}$ dislocation pair in one of the stable states identified above for pair interactions. The search space for stable configurations is then limited to just the relative (x_r, y_r) separation of dislocation pair 1 from dislocation pair 2. In Fig. 6, we show a variety of stable states for dislocation pairs in an $(m, n) = (14, 7)$ tube with $\theta = 0$ and constant separation $x = a\sqrt{3}/2$, $y = \pi R$ between the dislocations in each pair, each corresponding to state 3 in Fig. 2*B*. We initialize the two pairs of dislocation pairs at large x_r separation and then gradually probe the energy landscape by alternate gliding of the two dislocations in one of the pairs while the other pair is held fixed. By this means,

we identify the critical x_r separation at which the two dislocation pairs induce each other's relative glide motion, while each pair maintains the stable separation between its two dislocations.

Our simulations show that the dislocation pairs remain stable at any azimuthal separation when their x_r separation is large, $x_r > \pi R$ (black dots in Fig. 6*A*). Since each defect pair causes a kink in the tube axis, the azimuthal separation defines the resulting tube shape. At $y_r = \pi R$, for example, we obtain a double-kinked shape (state 1 in Fig. 6*A*) because the two pairs are oriented in opposite directions in the 3D embedding space, and thus the curvatures at the two kinks have opposite signs. However, if $x_r < a2\sqrt{3}$, the dislocation pairs become attractive and annihilate (state 2), which is possible because, at $y_r = \pi R$, they glide along the same pair of parastichies. The final state is then a straight, pristine tubular crystal.

Dislocations also move along the same glide parastichies when $y_r = 0$, but now their Burgers vectors become parallel in the 3D space. As a result, pairs of dislocation pairs are repulsive at small x_r and generate two identical kinks at larger separation (state 7). Intermediate azimuthal separations lead to stable helical shapes at large x_r (states 3 and 5). Helicity arises due to bending of the tube in a different direction at each kink. At smaller x_r, pairs repel for some y_r values but attract for others. Repulsion stabilizes the helical shape, whereas attraction stabilizes a small-x_r shape with a single kink (states 4 and 6). The latter case presents a pathway for a spontaneous shape transition from a helical to a kinked conformation, if a small perturbation were to destabilize the helical state.

In Fig. 6 *B* and *C*, we show energy profiles with respect to axial separation x_r at constant azimuthal separation y_r. The stable states (filled black circles) correspond to the stable states in Fig. 6*A*, whereas unstable states (empty circles) are marked by arrows in Fig. 6*A*. For $x_r \gtrsim \pi R$, we see an alternation of locally stable and unstable states revealing a slight energy barrier encountered in gliding one dislocation away from its partner by $\Delta x = \pm a$, before the partner takes a glide step in the same direction. The energy landscape of the pair of dislocation pairs thus resembles the periodic Peierls potential felt by an individual dislocation, under the assumption that the time between glide steps is always long compared to the timescale for elastic relaxation. Besides this small oscillation, the energy remains essentially constant at larger x_r.

However, for smaller initial separation $|x_r| < \pi R$, interactions between the two dislocation pairs overcome the energy barrier for glide steps, so that collective glide of the dislocation pair occurs spontaneously. For example, with a $y_r = 3a\sqrt{3}/2$ azimuthal separation between the two defect pairs, the two pairs approach until reaching the $x_r = 0$ state with a single kink (state 6, Fig. 6*B*). On the other hand, when $y_r = 0$, the two dislocation pairs repel at short distance until reaching a stable configuration at $x_r = 5a$ with two kinks of the same orientation (state 7, Fig. 6*C*).

Having found stable configurations and corresponding tube shapes among pairs of dislocation pairs, we can now design more complicated geometries by adding dislocation pair elements in a desired order. A series of stable dislocation pairs, arranged at constant (x_r, y_r) separation between consecutive pairs, creates repeating kinks along the tube. Fig. 7*A* depicts an $(m, n) = (13, 13)$ tube containing three metastable pairs with Burgers vector orientation $\theta = \pi/6$ relative to the tube axis. The first and third pairs are located on one side of the tube, whereas the middle pair is imposed on the opposite side ($y_r = \pi R$), and successive pairs have constant separation along the tube axis ($x_r = a\sqrt{3}$). The combined effect of the three dislocation pairs leads to a tube shape that approximates a helical deformation.

Larger deformations can be generated by imposing dislocations with Burgers vectors parallel to the tube axis ($\theta = 0$). In Fig. 7*B*, the $(m, n) = (14, 7)$ tube has 16 dislocations that are

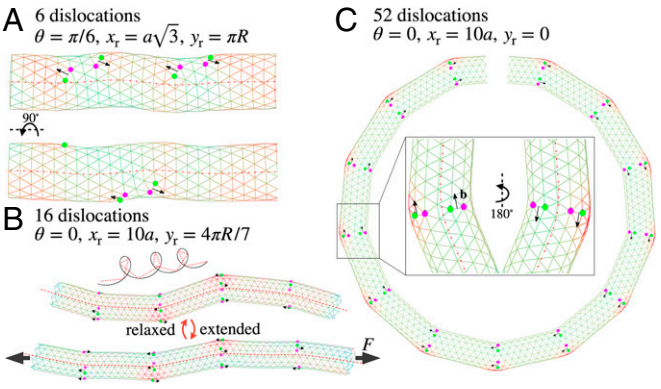

Fig. 7. Kinked tube shapes approximating continuously curved structures, obtained by imposing a series of metastable dislocation pair groups at uniform relative separation (x_r, y_r) and $\tilde{\kappa} = 0.1$. (*A* and *B*) Tube develops a quasi-helical shape of different pitch and radius depending on the positions and orientations of defects. In *B*, the helical tube demonstrates a significant reduction in stiffness compared to the pristine tube. (*C*) Bent toroidal conformations obtained by imposing a series of repeating dislocation groups along the tube with no relative rotation about the tube axis ($y_r = 0$). The parastichy numbers are $(m, n) = (13, 13)$ in *A* and $(14, 7)$ in *B* and *C*.

localized in four equally separated groups along the tube ($x_r = 10a$), each group consisting of two pairs and creating a large kink in the tube axis that corresponds to the absolutely stable state 6 in Fig. 6*A*. We impose dislocation groups at constant azimuthal separation ($y_r = 4\pi R/7$), which leads to rotations between successive kinks; as a result, the tube shape becomes approximately helical. The helical pitch and radius can be controlled by changing the rotation angle and separation between dislocation groups, and could even be varied along the length of the tube. The ratio between rotation angle and separation along the tube defines the torsion ($\sim y_r/x_r$), whereas the kink angle divided by separation approximates the curvature ($\sim c_{\mathrm{tot}}/x_r$) of the helical shape.

The helical macroscopic shape alters the mechanical response properties of the tube. As a proof of principle for this concept, we first examined a tube with a single group of four dislocations in the stable arrangement identified in Fig. 6*A*, state 6. We found that the tube's stiffness against small applied axial compression or tension, in the regime of Hookean elastic response, was reduced by 20% compared to a straight, pristine tube. The chosen dislocation pattern remains stable for imposed axial strains of up to 9%. We then tested a helical tube containing four groups of the same four-dislocation motif (Fig. 7*B*). The strain was applied, in this case, along the axis of the helix rather than the (spatially varying) local tube axis. This metastructure exhibits an ∼35% decrease of its stiffness compared to a pristine lattice. This significant reduction is caused by the increased number of dislocations in the tube as well as by the helical shape that can absorb the applied strain via torsion. Thus, we can expect that such dislocation-stabilized helical conformations could be used to create significantly compressible microscale springs even in materials with high Young's modulus.

If there is no azimuthal separation between consecutive defect groups, $y_r = 0$, then the tube bends in the same plane at each group (Fig. 7*C*), and, by imposing a series of metastable pairs, we obtain tube shapes that approximate continuously curved planar geometries, such as a ring in the case of the torus-like structure of Fig. 7*C*.

These kinked helices and rings are examples of a design pathway to shape a tubular crystal by localized curvature. Similarly to the mechanism of kink formation observed in multiwalled carbon nanotubes (69, 70), our findings show that mechanical equilibrium shapes can be obtained as a series of relatively straight segments connected at groups of stabilized dislocations.

Discussion

In this article, we have numerically demonstrated an emergent phenomenon of dislocation-mediated shape multistability in freestanding, flexible crystals of tubular geometry. Our simulations predict multiple metastable states restricting dislocation glide and causing macroscopic shape transitions, which make this system strikingly distinct from dislocations in a crystal attached to a rigid cylindrical substrate. We have explored this multistability by varying experimentally relevant design parameters for some chosen dislocation orientations and lattice helicity. Specifically, we found that changing the bending rigidity creates or eliminates certain metastable defect separations, and thus enables shape morphing into nontrivial tube conformations, by altering the localization of surface deformations around the dislocations. Additionally, we showed that an external bending force allows dynamical control of dislocation motion between distinct stable configurations, enabling shape multistability even when material properties such as $\tilde{\kappa}$ are fixed. We then demonstrated a principle of shape programming by which imposed dislocation patterns generate shape morphing into kinked shapes approximating targeted space curves.

The simulations presented in this work comprise just a few examples from a vast design space yet to be explored, opening multiple avenues for future investigations. Our approach can be generalized beyond dislocation groups with collinear Burgers vectors to collections of arbitrary dislocation orientations, generating new degrees of freedom and crossing glide paths. We have examined only a few sets of phyllotactic indices, focusing on achiral states for simplicity, and leaving for future work a systematic survey of (m, n) values—and coexisting sequences thereof—which may enable new tube shapes. We conjecture that chiral lattices will respond to bend in a manner that interpolates between our observations in the armchair and zigzag achiral tessellations, but that the response to imposed twist will change rapidly as (m, n) are varied (71). Even more generally, dislocation-mediated shape multistability can be sought in lattice types other than the triangular lattice considered here, especially honeycomb and rhombic tessellations as closer analogs to carbon nanotubes and microtobules. Unbound disclinations, while outside the scope of this study because of their higher energy, are expected to further enrich the dislocation interaction landscape, as they arise naturally on highly curved surfaces (28, 34) and have been shown to form coiled structures (72). Future exploration of these open questions will enable us to address the inverse problem: how to choose a prescribed defect pattern to obtain a desired, mechanically stable tube shape of arbitrary complexity.

Molecular dynamics (MD) simulations of freestanding tubular crystals will be important in extending our findings from the elastic networks explored here to objects with excluded volume, such as colloidal particles. Such a framework would also enable investigation of the role of assembly kinetics in forming dislocations, such as during colloidal assembly or, potentially, the assembly of tubulin dimers into protofilaments and MTs. Some effects that we have ignored for simplicity, such as thermal fluctuations and the Peierls potential, can be more naturally incorporated in the MD framework. Even though a freestanding crystal avoids in-surface stress by buckling, large stress or a grain boundary may still cause dissociation and/or nucleation of dislocations (29, 73). These possibilities are not examined in our elastic network model, and would be better investigated in the MD framework. Also, while we have assumed isotropic elasticity in this work, breaking this symmetry in the monomer interactions, or by introducing anisotropic bending rigidity (74) dependent on the orientations of the parastichies, will likely lead to new phenomena, for example, length-dependent rigidity (75), relevant to protein assemblies such as MTs.

An experimental realization of a freestanding tubular crystal could be obtained using, for example, colloidal particles with anisotropic surface potentials (76), or particles with anisotropic shape in an electric field (77), self-assembling into membranes with spontaneous curvature in one direction. Alternatively, a tubular crystal could be fabricated via assembly of its constituent units on a cylindrical substrate (21) and then removal of (dissolving of) the support. In the case of carbon nanotubes, temperature (78) and anisotropic catalytic activity (79, 80) can be used independently from one another to control the tube's growth front, allowing creation of a variety of shapes. Tubular structures obtained by methods such as these might spontaneously include defects, and, as a result, the existing dislocation pattern and the crystal shape will naturally adapt to changed constraints. Furthermore, dislocations can be generated or eliminated using, for example, optical fields (29, 30), through termination of individual parastichies at a growing edge (81), or by a designed embedding of particles with variable diameter (82). These techniques allow precise tailoring of desired patterns of defects that, in turn, cause changes in the lattice chirality (13), the strength (46), and the tube shape.

The distinctions that we have emphasized between the fixed cylindrical crystal and the freestanding tubular crystal highlight the need for new analytical approaches, incorporating the interplay of effective defect interactions and the curvature of the crystalline surface as it dynamically adapts to the defects' presence. Our geometrical approach to calculating the tube axis kink angle is a step forward in this regard. However, computational approaches remain necessary for calculating mechanically stable tube shapes in the 3D embedding space.

Inspired by the spherical crystal case, it is tempting to view the fixed-surface tubular crystal as a high-rigidity limit of the freestanding tubular crystal (33). As we have explored and exploited in this work, that assumption is not always correct: The tube axis in the freestanding case can change its orientation at the dislocation site, by whatever angle best relieves the stress induced by the dislocation, with no cost in extra strain at large distance. Therefore, the effective interactions between defects must incorporate the changes they induce in the crystalline membrane's embedding in the 3D space.

The feedback that we observe between surface deformations and in-surface defect dynamics suggests connections to be explored between this work and other topics of current interest in soft matter physics, including the stabilization of nonspherical droplet shapes in Pickering emulsions by packings of colloidal particles, often as crystals with many defects (83); motile disclinations in active matter on flexible, curved surfaces (84, 85); and complex out-of-plane deformations in nematic elastomers with imprinted defects (38, 39, 86). We hope that our findings will spur experimental investigations of colloidal freestanding tubular crystals, which are mesoscale analogs to carbon nanotubes and MTs, as a versatile platform for programmable, reconfigurable microwires with switchable mechanical and photonic response properties (87, 88).

Materials and Methods

Details of the Discrete Model. We consider a tubular crystal as a collection of nodes with positions $\mathbf{x}_i$ forming a 2D triangular lattice embedded in three spatial dimensions, with a preferred lattice spacing, a. Neighbor bonds, which would lie along lattice lines in a planar crystal, here lie along three families of helices. The geometry and chirality of a pristine (defect-free) tubular crystal can be conveniently defined using a pair of integer parastichy numbers (m, n), which give the number of distinct helices in the steepest right-handed and steepest left-handed families, respectively. Then the tube radius is defined by Eq. **2**. The orientation of the lattice depends on the angle between the steepest left-handed helix and the cylinder axis as $\tan\phi \approx \frac{2}{\sqrt{3}}\left(\frac{m}{n} - \frac{1}{2}\right)$ (Fig. 1) (26).

The discrete elastic energy of the tubular crystal is given by Eq. **1**. The local curvature at each node is computed as $G_i^2 = 4(H_i)^2 - 2K_i$, where the Gaussian curvature $K_i = (2\pi - \sum \rho_j)/A_i$ is expressed through the angles

between two adjacent edges $\rho_j = \angle(l_{ij}, l_{ij+1})$, and the mean curvature $H_i = ||\sum_j((\mathbf{x}_i - \mathbf{x}_j)(\cot\psi_{ij}^1 + \cot\psi_{ij}^2))||/(4A_i)$ is defined over the adjacent edges, where ψ_{ij}^{α} $(\alpha = 1, 2)$ are the two angles opposite to the edge in the two triangles sharing the edge l_{ij}. Here, $A_i = \sum_j \mathcal{A}_j/3$ is the observed area around a node i, which is calculated using the areas $\mathcal{A}_j$ of the adjacent triangular faces. We choose the reference state to be a pristine triangular lattice with uniform spacing $l_{ij} = a$. In this state, the elastic energy comprises only the bending energy, which depends on the cylinder radius R and length L as $\hat{\mathcal{F}}_b \to \pi\kappa L/R$.

To account for nonzero spontaneous curvature, we slightly modify Eq. **1**. We first calculate discrete mean and Gaussian curvatures, and, from these, calculate the discrete principal curvatures as $k_{\{1,2\}i} = H_i \pm \sqrt{H_i^2 - K_i}$. The local curvature energy density of Eq. **1** is then replaced by $(\kappa/2)[(k_{1i} - H_0^2)^2 + k_{2i}^2]$, always choosing $k_{1i} \geq k_{2i}$.

We assume overdamped dynamics, and the position $\mathbf{x}_i$ of node i changes to minimize the elastic energy following the pseudotime evolution equations $\gamma\partial\mathbf{x}_i/\partial t = -\delta\mathcal{F}_e/\delta\mathbf{x}_i$. Here, γ is the friction coefficient associated with energy dissipation during relaxation of the elastic energy. For a given bond network, we allow the system to relax to an equilibrium configuration by minimizing the elastic energy over the node positions until the relative reduction in energy per update step becomes smaller than 10^{-7}.

A single dislocation can be inserted by removing or adding a row of nodes to the lattice up to one end of the tube, such that the lattice remains pristine (six-coordinated) everywhere except at the dislocation, which consists of two nodes with five and seven neighbors, respectively. Such a defect in a crystalline structure can be characterized by the Burgers vector connecting the gap in the Burgers circuit around the defect, $\mathbf{b} = -\oint(\partial\mathbf{u}/\partial l)dl$, where $\mathbf{u}$ is the displacement vector. A dislocation pair nucleation can be imposed by a single bond flip that removes a bond between neighboring nodes and replaces it with a new bond normal to it, thus creating two pairs of nodes with five and seven neighbors. We validated our computational approach by reproducing the results of ref. 36 for critical bending rigidity at which a single dislocation causes a crystalline membrane to buckle. A dislocation glide move by one lattice spacing to a neighboring node is accomplished by a similar bond flip.

We assume a separation of timescales such that the elastic energy is completely relaxed to a state of mechanical equilibrium between consecutive glide moves. The direction of gliding is chosen to decrease the total elastic energy and can be along or opposite the Burgers vector, or the defect can remain at the same position if it is a stable configuration, depending on interaction with other defects, the tube shape, and external stresses.

This procedure gives rise to an effective energy landscape for the dislocations on the tubular crystal, whose local minima we explore in this work. For tubes with multiple dislocations, this landscape becomes high-dimensional and difficult to minimize rigorously, as each test glide move requires a full minimization of the elastic energy. Therefore, we examine stability by choosing a defect at random and performing a "trial" dislocation glide in both directions, along and opposite to the Burgers vector; we then keep the configuration with the lowest total energy. If the given position of a defect is stable, that is, any glide causes an increase in the total energy, then the dislocation is excluded from the next random selection until another defect is subject to glide, and the bond network changes. This procedure continues while there are defects in the lattice, and any possible dislocation glide step leads to a more preferable energy state. Otherwise, if all defects have been removed or are in a stable position, the configuration is considered to be at equilibrium. In our simulations, we ignore the Peierls barrier during each glide step, assuming that thermal fluctuations enable the exploration of glide moves that we undertake quasi-deterministically. However, fully stochastic update rules or simultaneous glide might lead to other mechanically stable configurations that cannot be reached with our approach.

Computation of the Local Tube Radius. The local radius R_i at a node i is calculated as the shortest distance between the node and the centerline of the tube, C. The centerline can, in general, significantly deviate from the axis in a pristine tube and have kinks along it due to dislocations. For tubes with a small deviation of the tube axis from the coordinate axis OX, we calculate the position of the centerline at discrete points lying in evenly separated parallel cross-sections of the tube with the normal vector along OX. Position $C(y, z)$ at each fixed x is found as the equilibrium position where the y and z components of a fictitious repulsive force, exerted by all nodes in the lattice, vanish (26). The force from each node R_j is oriented toward $C(y, z)$ and has a power-law form, with amplitude decaying with the distance to a node as $|R_j - C(y, z)|^{-8}$. The separation between cross-sections is chosen to be small ($0.01a$), allowing a dense discretization of the centerline. Then the local radius R_i is computed as the distance to the nearest point on $C(x, y, z)$. In case of large deviations of the tube axis from OX, we calculate C in cross-sections constructed in a local frame rotated such that the local OX coincides with the tangent of C calculated at the previous step. This ensures small separation between points along C.

Data Availability. C/C++ source code.dat files (XYZ coordinates) have been deposited in datadryad.org (https://datadryad.org/stash/dataset/doi:10.6071/M3196R). The dataset has been assigned DOI:10.6071/M3196R.

ACKNOWLEDGMENTS. We thank Kinjal Dasbiswas and David R. Nelson for helpful comments. We gratefully acknowledge computing time on the Multi-Environment Computer for Exploration and Discovery cluster at University of California, Merced, which was funded by NSF Grant ACI-1429783.

1. A. Thess *et al.*, Crystalline ropes of metallic carbon nanotubes. *Science* **273**, 483–487 (1996).
2. A. Klug, The tobacco mosaic virus particle: Structure and assembly. *Philos. Trans. R. Soc. London Ser. B: Biol. Sci* **354**, 531–535 (1999).
3. E. Nogales, Structural insight into microtubule function. *Annu. Rev. Biophys. Biomol. Struct.* **30**, 397–420 (2001).
4. M. Tymczenko *et al.*, Colloidal crystal wires. *Adv. Mater.* **20**, 2315–2318 (2008).
5. B. Yakobson, Mechanical relaxation and "intramolecular plasticity" in carbon nanotubes. *Appl. Phys. Lett.* **72**, 918–920 (1998).
6. I. Adler, D. Barabe, R. V. Jean, A history of the study of phyllotaxis. *Ann. Biol.* **80**, 231–244 (1997).
7. M. F. Pennybacker, P. D. Shipman, A. C. Newell, Phyllotaxis: Some progress, but a story far from over. *Phys. D* **306**, 48–81 (2015).
8. F. Li, X. Badel, J. Linnros, J. B. Wiley, Fabrication of colloidal crystals with tubular-like packings. *J. Am. Chem. Soc.* **127**, 3268–3269 (2005).
9. J. F. Sadoc, N. Rivier, J. Charvolin, Phyllotaxis: A non-conventional crystalline solution to packing efficiency in situations with radial symmetry. *Acta Crystallogr. A* **68**, 470–483 (2012).
10. Y. Guo, B. G. P. van Ravensteijn, W. K. Kegel, Self-assembly of isotropic colloids into colloidal strings, Bernal spiral-like, and tubular clusters. *Chem. Commun. (Camb.)* **56**, 6309–6312 (2020).
11. T. Li *et al.*, Self-assembled nanoparticle supertubes as robust platform for revealing long-term, multiscale lithiation evolution. *Matter* **1**, 976–987 (2019).
12. M. A. Lohr *et al.*, Helical packings and phase transformations of soft spheres in cylinders. *Phys. Rev. E Stat. Nonlin. Soft Matter Phys.* **81**, 040401 (2010).
13. W. F. Harris, R. O. Erickson, Tubular arrays of spheres: Geometry, continuous and discontinuous contraction, and the role of moving dislocations. *J. Theor. Biol.* **83**, 215–246 (1980).
14. K. Suenaga *et al.*, Imaging active topological defects in carbon nanotubes. *Nat. Nanotechnol.* **2**, 358–360 (2007).
15. D. Chrétien, F. Metoz, F. Verde, E. Karsenti, R. H. Wade, Lattice defects in microtubules: Protofilament numbers vary within individual microtubules. *J. Cell Biol.* **117**, 1031–1040 (1992).
16. A. Mughal, H. K. Chan, D. Weaire, Phyllotactic description of hard sphere packing in cylindrical channels. *Phys. Rev. Lett.* **106**, 115704 (2011).
17. D. Wood, C. Santangelo, A. Dinsmore, Self-assembly on a cylinder: A model system for understanding the constraint of commensurability. *Soft Matter* **9**, 10016–10024 (2013).
18. A. Mughal, D. Weaire, Theory of cylindrical dense packings of disks. *Phys. Rev. E Stat. Nonlin. Soft Matter Phys.* **89**, 042307 (2014).
19. L. Fu, W. Steinhardt, H. Zhao, J. E. Socolar, P. Charbonneau, Hard sphere packings within cylinders. *Soft Matter* **12**, 2505–2514 (2016).
20. J. Winkelmann, B. Haffner, D. Weaire, A. Mughal, S. Hutzler, Simulation and observation of line-slip structures in columnar structures of soft spheres. *Phys. Rev. E* **96**, 012610 (2017).
21. N. Tanjeem, W. H. Wilkin, D. A. Beller, C. H. Rycroft, V. N. Manoharan, Geometrical frustration and defect formation in growth of colloidal nanoparticle crystals on a cylinder: Implications for assembly of chiral nanomaterials. *ACS Appl. Nano Mater.* **4**, 10682–10691 (2021).
22. J. H. Moon, S. Kim, G. R. Yi, Y. H. Lee, S. M. Yang, Fabrication of ordered macroporous cylinders by colloidal templating in microcapillaries. *Langmuir* **20**, 2033–2035 (2004).
23. C. Nisoli, N. M. Gabor, P. E. Lammert, J. D. Maynard, V. H. Crespi, Static and dynamical phyllotaxis in a magnetic cactus. *Phys. Rev. Lett.* **102**, 186103 (2009).
24. C. Nisoli, N. M. Gabor, P. E. Lammert, J. D. Maynard, V. H. Crespi, Annealing a magnetic cactus into phyllotaxis. *Phys. Rev. E Stat. Nonlin. Soft Matter Phys.* **81**, 046107 (2010).
25. A. Amir, J. Paulose, D. R. Nelson, Theory of interacting dislocations on cylinders. *Phys. Rev. E Stat. Nonlin. Soft Matter Phys.* **87**, 042314 (2013).
26. D. A. Beller, D. R. Nelson, Plastic deformation of tubular crystals by dislocation glide. *Phys. Rev. E* **94**, 033004 (2016).
27. B. I. Dunlap, Constraints on small graphitic helices. *Phys. Rev. B Condens. Matter* **50**, 8134–8137 (1994).
28. M. J. Bowick, L. Giomi, Two-dimensional matter: Order, curvature and defects. *Adv. Phys.* **58**, 449–563 (2009).
29. F. A. Lavergne, A. Curran, D. G. A. L. Aarts, R. P. A. Dullens, Dislocation-controlled formation and kinetics of grain boundary loops in two-dimensional crystals. *Proc. Natl. Acad. Sci. U.S.A.* **115**, 6922–6927 (2018).

30. W. T. Irvine, A. D. Hollingsworth, D. G. Grier, P. M. Chaikin, Dislocation reactions, grain boundaries, and irreversibility in two-dimensional lattices using topological tweezers. *Proc. Natl. Acad. Sci. U.S.A.* **110**, 15544–15548 (2013).
31. C. E. Cash *et al.*, Local melting attracts grain boundaries in colloidal polycrystals. *Phys. Rev. Lett.* **120**, 018002 (2018).
32. A. R. Bausch *et al.*, Grain boundary scars and spherical crystallography. *Science* **299**, 1716–1718 (2003).
33. J. Lidmar, L. Mirny, D. R. Nelson, Virus shapes and buckling transitions in spherical shells. *Phys. Rev. E Stat. Nonlin. Soft Matter Phys.* **68**, 051910 (2003).
34. V. Vitelli, J. B. Lucks, D. R. Nelson, Crystallography on curved surfaces. *Proc. Natl. Acad. Sci. U.S.A.* **103**, 12323–12328 (2006).
35. P. W. Ellis *et al.*, Curvature-induced defect unbinding and dynamics in active nematic toroids. *Nat. Phys.* **14**, 85–90 (2018).
36. H. S. Seung, D. R. Nelson, Defects in flexible membranes with crystalline order. *Phys. Rev. A Gen. Phys.* **38**, 1005–1018 (1988).
37. T. Zhang, X. Li, H. Gao, Defects controlled wrinkling and topological design in graphene. *J. Mech. Phys. Solids* **67**, 2–13 (2014).
38. C. Modes, K. Bhattacharya, M. Warner, Gaussian curvature from flat elastica sheets. *Proc.- Royal Soc. Math. Phys. Eng. Sci.* **467**, 1121–1140 (2011).
39. A. P. Zakharov, L. M. Pismen, Reshaping nemato-elastic sheets. *Eur. Phys. J. E Soft Matter* **38**, 75 (2015).
40. L. Giomi, M. J. Bowick, Elastic theory of defects in toroidal crystals. *Eur. Phys. J. E* **27**, 275–296 (2008).
41. J. P. Hirth, J. Lothe, *Theory of Dislocations* (Wiley, New York, NY, 1982).
42. Y. Klein, E. Efrati, E. Sharon, Shaping of elastic sheets by prescription of non-Euclidean metrics. *Science* **315**, 1116–1120 (2007).
43. A. S. Gladman, E. A. Matsumoto, R. G. Nuzzo, L. Mahadevan, J. A. Lewis, Biomimetic 4D printing. *Nat. Mater.* **15**, 413–418 (2016).
44. H. Aharoni, Y. Xia, X. Zhang, R. D. Kamien, S. Yang, Universal inverse design of surfaces with thin nematic elastomer sheets. *Proc. Natl. Acad. Sci. U.S.A.* **115**, 7206–7211 (2018).
45. R. H. Baughman *et al.*, Carbon nanotube actuators. *Science* **284**, 1340–1344 (1999).
46. A. Takakura *et al.*, Strength of carbon nanotubes depends on their chemical structures. *Nat. Commun.* **10**, 3040 (2019).
47. K. Akagi, R. Tamura, M. Tsukada, S. Itoh, S. Ihara, Electronic structure of helically coiled cage of graphitic carbon. *Phys. Rev. Lett.* **74**, 2307–2310 (1995).
48. Y. Zhao, J. Wei, R. Vajtai, P. M. Ajayan, E. V. Barrera, Iodine doped carbon nanotube cables exceeding specific electrical conductivity of metals. *Sci. Rep.* **1**, 83 (2011).
49. S. Smart, A. Cassady, G. Lu, D. Martin, The biocompatibility of carbon nanotubes. *Carbon* **44**, 1034–1047 (2006).
50. A. Fabbro, G. Cellot, M. Prato, L. Ballerini, Interfacing neurons with carbon nanotubes: (Re)engineering neuronal signaling. *Prog. Brain Res.* **194**, 241–252 (2011).
51. K. Jiang, Q. Li, S. Fan, Nanotechnology: Spinning continuous carbon nanotube yarns. *Nature* **419**, 801 (2002).
52. B. Vigolo *et al.*, Macroscopic fibers and ribbons of oriented carbon nanotubes. *Science* **290**, 1331–1334 (2000).
53. F. Xu, X. Wang, Y. Zhu, Y. Zhu, Wavy ribbons of carbon nanotubes for stretchable conductors. *Adv. Funct. Mater.* **22**, 1279–1283 (2012).
54. F. J. Nédélec, T. Surrey, A. C. Maggs, S. Leibler, Self-organization of microtubules and motors. *Nature* **389**, 305–308 (1997).
55. T. Torisawa, D. Taniguchi, S. Ishihara, K. Oiwa, Spontaneous formation of a globally connected contractile network in a microtubule-motor system. *Biophys. J.* **111**, 373–385 (2016).
56. C. P. Brangwynne, F. C. MacKintosh, D. A. Weitz, Force fluctuations and polymerization dynamics of intracellular microtubules. *Proc. Natl. Acad. Sci. U.S.A.* **104**, 16128–16133 (2007).
57. R. Martel, H. R. Shea, P. Avouris, Rings of single-walled carbon nanotubes. *Nature* **398**, 299 (1999).
58. C. Janke, G. Montagnac, Causes and consequences of microtubule acetylation. *Curr. Biol.* **27**, R1287–R1292 (2017).
59. V. Hunyadi, D. Chrétien, H. Flyvbjerg, I. M. Jánosi, Why is the microtubule lattice helical? *Biol. Cell* **99**, 117–128 (2007).
60. T. A. Witten, Stress focusing in elastic sheets. *Rev. Mod. Phys.* **79**, 643 (2007).
61. R. O. Erickson, Tubular packing of spheres in biological fine structure. *Science* **181**, 705–716 (1973).
62. L. D. Landau, E. M. Lifshits, *Theory of Elasticity* (Pergamon, New York, NY, 1986).
63. L. Schaedel *et al.*, Lattice defects induce microtubule self-renewal. *Nat. Phys.* **15**, 830–838 (2019).
64. A. Plummer, D. R. Nelson, Buckling and metastability in membranes with dilation arrays. *Phys. Rev. E* **102**, 033002 (2020).
65. P. Lipowsky, M. J. Bowick, J. H. Meinke, D. R. Nelson, A. R. Bausch, Direct visualization of dislocation dynamics in grain-boundary scars. *Nat. Mater.* **4**, 407–411 (2005).
66. G. J. Brouhard, L. M. Rice, The contribution of $\alpha\beta$-tubulin curvature to microtubule dynamics. *J. Cell Biol.* **207**, 323–334 (2014).
67. G. M. Alushin *et al.*, The Ndc80 kinetochore complex forms oligomeric arrays along microtubules. *Nature* **467**, 805–810 (2010).
68. E. M. Wilson-Kubalek, I. M. Cheeseman, C. Yoshioka, A. Desai, R. A. Milligan, Orientation and structure of the Ndc80 complex on the microtubule lattice. *J. Cell Biol.* **182**, 1055–1061 (2008).
69. X. Zhang *et al.*, The texture of catalytically grown coil-shaped carbon nanotubules. *Europhys. Lett.* **27**, 141 (1994).
70. D. Bernaerts *et al.*, Electron microscopy study of coiled carbon tubules. *Philos. Mag. A Phys. Condens. Matter Struct. Defects Mech. Prop.* **71**, 605–630 (1995).
71. D. B. Zhang, R. D. James, T. Dumitrică, Dislocation onset and nearly axial glide in carbon nanotubes under torsion. *J. Chem. Phys.* **130**, 071101 (2009).
72. S. Ihara, S. Itoh, Ji. Kitakami, Helically coiled cage forms of graphitic carbon. *Phys. Rev. B Condens. Matter* **48**, 5643–5647 (1993).
73. J. Y. Huang *et al.*, Kink formation and motion in carbon nanotubes at high temperatures. *Phys. Rev. Lett.* **97**, 075501 (2006).
74. J. A. Tuszyński, T. Luchko, S. Portet, J. M. Dixon, Anisotropic elastic properties of microtubules. *Eur Phys J E Soft Matter* **17**, 29–35 (2005).
75. A. Kis *et al.*, Nanomechanics of microtubules. *Phys. Rev. Lett.* **89**, 248101 (2002).
76. Z. Zhang, S. C. Glotzer, Self-assembly of patchy particles. *Nano Lett.* **4**, 1407–1413 (2004).
77. J. J. Crassous *et al.*, Field-induced assembly of colloidal ellipsoids into well-defined microtubules. *Nat. Commun.* **5**, 5516 (2014).
78. Y. Yao *et al.*, Temperature-mediated growth of single-walled carbon-nanotube intramolecular junctions. *Nat. Mater.* **6**, 283–286 (2007).
79. S. Amelinckx *et al.*, A formation mechanism for catalytically grown helix-shaped graphite nanotubes. *Science* **265**, 635–639 (1994).
80. N. Mubarak, E. Abdullah, N. Jayakumar, J. Sahu, An overview on methods for the production of carbon nanotubes. *J. Ind. Eng. Chem.* **20**, 1186–1197 (2014).
81. H. Doodhi *et al.*, Termination of protofilament elongation by eribulin induces lattice defects that promote microtubule catastrophes. *Curr. Biol.* **26**, 1713–1721 (2016).
82. B. VanSaders, S. C. Glotzer, Sculpting crystals one Burgers vector at a time: Toward colloidal lattice robot swarms. *Proc. Natl. Acad. Sci. U.S.A.* **118**, e2017377118 (2021).
83. Z. Xie, C. J. Burke, B. Mbanga, P. T. Spicer, T. J. Atherton, Geometry and kinetics determine the microstructure in arrested coalescence of Pickering emulsion droplets. *Soft Matter* **15**, 9587–9596 (2019).
84. F. C. Keber *et al.*, Topology and dynamics of active nematic vesicles. *Science* **345**, 1135–1139 (2014).
85. Y. Maroudas-Sacks *et al.*, Topological defects in the nematic order of actin fibres as organization centres of *Hydra* morphogenesis. *Nat. Phys.* **17**, 251–259 (2020).
86. V. Gimenez-Pinto, F. Ye, B. Mbanga, J. V. Selinger, R. L. B. Selinger, Modeling out-of-plane actuation in thin-film nematic polymer networks: From chiral ribbons to auto-origami boxes via twist and topology. *Sci. Rep.* **7**, 45370 (2017).
87. S. H. Kim, H. Hwang, S. M. Yang, Fabrication of robust optical fibers by controlling film drainage of colloids in capillaries. *Angew. Chem. Int. Ed. Engl.* **51**, 3601–3605 (2012).
88. M. J. Solomon, Tools and functions of reconfigurable colloidal assembly. *Langmuir* **34**, 11205–11219 (2018).